Optimal isotropic, reusable truss lattice material with near-zero Poisson's ratio

Xueyan Chen[a,b], Johnny Moughames[b], Qingxiang Ji[a,b], Julio Andrés Iglesias Martínez[b], Huifeng Tan[a,*], Samia Adrar[b], Nicolas Laforge[b], Jean-Marc Cote[b], Sébastien Euphrasie[b], Gwenn Ulliac[b], Muamer Kadic[b], and Vincent Laude[b]

[a] *National Key Laboratory of Science and Technology on Advanced Composites in Special Environments, Harbin Institute of Technology; 92 Xidazhi Street, Harbin, 150001, PR China*

[b] *Institut FEMTO-ST, CNRS, Université Bourgogne Franche-Comté, 25000 Besançon, France*

Abstract

Cork is a natural amorphous material with near-zero Poisson's ratio that is ubiquitously used for sealing glass bottles. It is an anisotropic, transversally isotropic, composite that can hardly be scaled down. Here, we propose a new class of isotropic and reusable cork-like metamaterial that is designed from a hybrid truss-lattice material to show an isotropic Poisson's ratio close to zero. Optimization is conducted using a multi-objective genetic algorithm, assisted by an elliptical basis function neural network, and coupled with finite element simulations. The optimal micro-structured metamaterial, fabricated by two-photon lithography with a lattice constant of 300 μm, has an almost isotropic Poisson's ratio smaller than 0.08 in all directions. It can recover 96.6% of its original shape after a compressional test exceeding 20% strain.

Keywords: isotropic composite; reusable material; near-zero Poisson's ratio; optimal design; truss lattice materials

1. Introduction

Poisson's ratio υ is defined as the negative ratio of transverse to longitudinal strain [1]. For a stable, isotropic and linear elastic material, Poisson's ratio is bound to remain between -1 [2, 3], corresponding to 'dilational' or auxetic materials, and 0.5, a limit defining the 'incompressible' solid set by a positive energy requirement [4, 5]. In nature, most conventional isotropic materials have a positive Poisson's ratio. Rubber, as well as most liquids, exhibits a Poisson's ratio of nearly 0.5. Rigid metals and polymers as a rule have a poisson's ratio ranging between 0.2 and 0.45 [2, 6]. For other soft metals and polymers, Poisson's ratio is usually between 0.33 and 0.5. By contrast, only a few natural materials such as bone have negative Poisson's ratio [7].

Recent advances in topological structural design have enabled the enlargement of the family of isotropic auxetics [8]. Carta *et al.* utilized threefold symmetry of the arrangement of voids to design a two-dimensional porous isotropic auxetic solid [9]. By embedding random re-entrant inclusions into a matrix, Hou *et al.* developed 2D composite structures with isotropic negative Poisson's ratio [10]. Combining the symmetry of a cubic lattice and that of additional diagonal elements, Cabras *et al.* presented a class of pin-jointed auxetic three-dimensional isotropic lattice material [11]. Furthermore, by adopting finite small connections, Bückmann *et al.* designed, fabricated and characterized a three-dimensional auxetic isotropic metamaterial reaching an ultimate Poisson's ratio of -0.8 [8]. Lately, Frenzel et al. used auxetics combined with chirality to observe acoustical activity [12, 13].

Isotropic structural materials with positive Pois-

[1] tanhf@hit.edu.cn

son's ratio are generally designed for bearing different types of mechanical loads [14–17] or absorbing energy [18]. The most popular way to optimise isotropy is to combine different structures in order to increase the number of equivalent directions and thus, via geometry increase, isotropy [15, 19–22]. Gurtner *et al.* proposed the first optimal and isotropic three-dimensional truss-lattice structure [15]. Tancogne *et al.* further formulated analytical conditions on the lattice topology to achieve elastic isotropy [19] and studied the effect of bending ratio to axial stiffness of the micro-strut on structural isotropy [20]. Bonatti *et al.* recently reported a family of elastically-isotropic shell-lattice materials whose Young's modulus is always higher than that of optimal isotropic truss-lattices and approaches the Hashin–Shtrikman bound at high relative densities [18]. Berger *et al.* presented a class of cubic-octet hybrid closed foams achieving the Hashin–Shtrikman upper bounds on isotropic elastic stiffness [16]. Tancogne *et al.* identified a class of low-density plate-lattice metamaterial showing optimal isotropic stiffness and nearly isotropic yield strength [17].

Cork, a conventional natural material, is emblematic among near-zero Poisson's ratio materials [23–25]. It shows very little lateral expansion when compressed and is widely used to seal bottles, especially for wine. As a composite, it is almost transversally isotropic and its Poisson's ratio is indeed a symmetric tensor. Independent Poisson's ratio constants $\upsilon_{12} = 0.097$, $\upsilon_{13} = 0.064$, and $\upsilon_{23} = 0.26$ have been reported for cork [24]. Polymeric foams may have been the earliest case for lightweight isotropic material with a Poisson's ratio smaller than 0.1 in modulus [6, 26]. Their fabrication technique, however, differs significantly from current 3D printing technologies. With the new additive manufacturing techniques it is extremely difficult to program and print random structures such as foams and periodic motifs are hence preferred [27–36]. Recently, some efforts were made to design isotropic zero Poisson's ratio materials. Based on truss or thin frame beam theory, Sigmund presented a three dimensional optimal structure with zero Poisson's ratio [37]. Starting from a different structure, Guth *et al.* proposed another kind of 3D pin-jointed structure [38]. However, those well-designed isotropic structures have not been validated experimentally thus far. Moreover, subject to limitations of numerical algorithms, the effect of the nodal overlapping volume was not considered, which we find seriously influences mechanical properties, including isotropy and Poisson's ratio.

In this paper, we aim at designing an isotropic near-zero Poisson's ratio material based on a periodic microstructure with cubic symmetry, that can be scaled easily and fabricated additively. We base our design on the hybrid truss lattice structure of Fig. 1

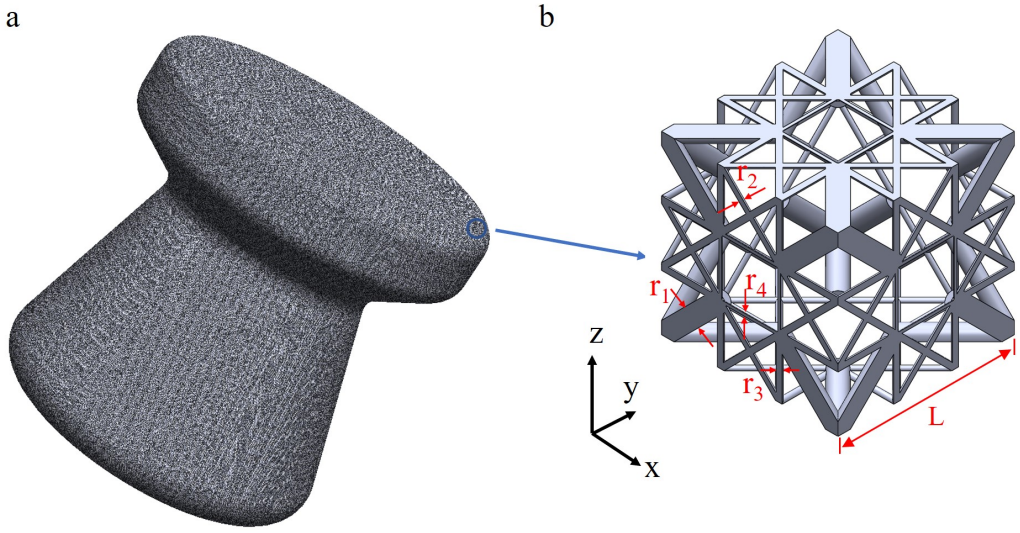

Figure 1: Principle of the truss lattice material with near-zero Poisson's ratio. (a) Artistic illustration of a truss lattice bottle stopper and (b) corresponding representive unit cell with geometrical parameters indicated.

that was first presented by Sigmund [37]. The unit cell follows simple cubic symmetry. Isotropy and near-zero Poisson's ratio are set as goals of a multi-objective optimization procedure where the radii of the struts are the optimized parameters. Optimization results in an almost isotropic design with Poisson's ratio less than 0.08 in all directions. Samples are printed using two-photon polymerization at a lattice constant of 300 μm in two different crystallographic directions, [100] and [110]. Uniaxial compression tests confirm the isotropic near-zero Poisson's ratio but also the recovery of the material after enduring strains up to 20%. Such a mechanical behavior thus makes it potentially attractive for product protection and goods packaging. When suffering from impact loading, limiting stress can pass through the protection toward the product. The layer-by-layer buckling failure mode will further enhance this protection ability. Moreover, the recovery ability can save space for packaging which is important in aerospace applications.

2. Evaluation of isotropy and Poisson's ratio

The constitutive law of linear elasticity of three-dimensional composites relates the stress tensor $\boldsymbol{\sigma}$ to the strain tensor $\boldsymbol{\epsilon}$ via an effective order-4 symmetric stiffness tensor $\boldsymbol{C}$ as

$$\boldsymbol{\sigma} = \boldsymbol{C} : \boldsymbol{\epsilon}, \tag{1}$$

where $C_{ijkl} = C_{klij} = C_{jilk}$. For lattice materials with simple-cubic symmetry [8, 39], the effective stiffness tensor has only three independent elements and can be rewritten in Voigt notation [40],

$$\boldsymbol{C} = \begin{bmatrix} C_{11} & C_{12} & C_{12} & 0 & 0 & 0 \\ & C_{11} & C_{12} & 0 & 0 & 0 \\ & & C_{11} & 0 & 0 & 0 \\ & & & C_{44} & 0 & 0 \\ & sym & & & C_{44} & 0 \\ & & & & & C_{44} \end{bmatrix}. \tag{2}$$

Using the Christofell equation for elastic waves [41, 42], the independent stiffness elements can be expressed using the effective mass density and phase velocities in selected directions of propagation. The effective mass density ρ is defined as the product of volume filling fraction f by the mass density ρ_0 of the constituent material [43]. Only three phase velocities v are required to identify all three independent stiffness constants. We consider the three bulk waves in direction [110]. One is a pure-shear wave S1 polarized along direction [001], the other two are quasi-longitudinal L and quasi-shear S2 waves with mixed polarization in the (x, y) plane. For propagation in direction [110], the Christofell equation leads to [8, 44]

$$C_{44} = \rho v_{\mathrm{S1}}^2, \tag{3}$$

$$C_{12} = \rho v_{\mathrm{L}}^2 - \rho v_{\mathrm{S1}}^2 - \rho v_{\mathrm{S2}}^2, \tag{4}$$

$$C_{11} = \rho v_{\mathrm{L}}^2 - \rho v_{\mathrm{S1}}^2 + \rho v_{\mathrm{S2}}^2. \tag{5}$$

For propagation along direction [100], Eq. (3) would be unchanged whereas Eq. (5) would give $C_{11} = \rho v_L^2$. Isotropy requires velocity to be independent of the direction of propagation and hence implies

$$v_{\mathrm{S1}} = v_{\mathrm{S2}} \ \text{ along direction [110]}. \tag{6}$$

Reciprocally, if Eq. (6) holds then there are only two independent stiffness constants instead of three and the stiffness tensor is isotropic. As a whole, Eq. (6) is a necessary and sufficient condition for isotropy. Poisson's ratio for compression along the principal axes can be expressed as [45, 46]

$$\upsilon = \frac{C_{12}}{C_{11} + C_{12}}. \tag{7}$$

Hence, we can estimate Poisson's ratio in direction [110] using the following formula

$$\upsilon = \frac{v_{\mathrm{L}}^2 - v_{\mathrm{S1}}^2 - v_{\mathrm{S2}}^2}{2(v_{\mathrm{L}}^2 - v_{\mathrm{S1}}^2)}, \tag{8}$$

where velocities are measured along direction [110]. If isotropy is simultaneouly achieved, formula (8) is valid for all directions of propagation.

In practice, velocities are obtained numerically using a finite element model of the unit cell in Fig. 1(b) subjected to Bloch periodic boundary conditions. A small wavenumber $k = \pi/(100L)$ is considered along direction [110] and eigenfrequencies are obtained. The three lowest eigenfrequencies, when divided by k, give velocities v_{S1}, v_{S2} and v_{L}; they are readily classified as longitudinal or shear by comparing the polarization of the eigenfunctions.

We note another useful expression for the Poisson's ratio for cubic symmetry that is valid for an arbitrary compression direction [8, 47, 48].

$$\upsilon(\phi,\theta) = -\frac{Ar_{12} + B(r_{44} - 2)}{16[C + D(2r_{12} + r_{44})]} \tag{9}$$

with

$$r_{12} = \frac{S_{12}}{S_{11}}, \tag{10}$$

$$r_{44} = \frac{S_{44}}{S_{11}}, \tag{11}$$

$$A = 2[53 + 4\cos(2\theta) + 7\cos(4\theta) + 8\cos(4\phi)\sin^4(\theta)], \tag{12}$$

$$B = -11 + 4\cos(2\theta) + 7\cos(4\theta) + 8\cos(4\phi)\sin^4(\theta), \tag{13}$$

$$C = 8\cos^4(\theta) + 6\sin^4(\theta) + 2\cos(4\phi)\sin^4(\theta), \tag{14}$$

$$D = 2[\sin^2(2\theta) + \sin^4(\theta) + \sin^4(2\phi)], \tag{15}$$

where (θ, ϕ) are the azimuthal and polar angles in spherical coordinates. The compliance tensor $\boldsymbol{S}$ is the inverse of the stiffness tensor $\boldsymbol{C}$.

3. Optimization of the structure

3.1. Optimization strategy

The cubic-symmetry truss lattice structure of Fig. 1 was selected for optimization. The corresponding representative unit cell model contains 64 struts of four different types. The unit cell length L being fixed to 300 µm, there are four geometrical parameters, (r_1, r_2, r_3, r_4), available for optimization. The ranges of the design parameters were fixed as $14\,\mu\text{m} \le r_1 \le 16\,\mu\text{m}$, $4\,\mu\text{m} \le r_2 \le 6\,\mu\text{m}$, $4\,\mu\text{m} \le r_3 \le 6\,\mu\text{m}$, and $2\,\mu\text{m} \le r_4 \le 4\,\mu\text{m}$. Note that we adopt a geometry type similar to Sigmund's [37], but with completely different geometrical parameters. The ranges of the parameters are selected to satisfy the requirement of elastic buckling and the limitations of the 3D printer (Direct Laser Writing by Nanoscribe). Compared with the structure originally proposed by Sigmund, we consider larger values for r_1 but smaller values for r_2, r_3, and r_4.

Fig. 2 illustrates the detailed flowchart for optimization. The optimization problem aims at simultaneously imposing the isotropy condition (6) and minimizing Poisson's ratio (8). The objective functions

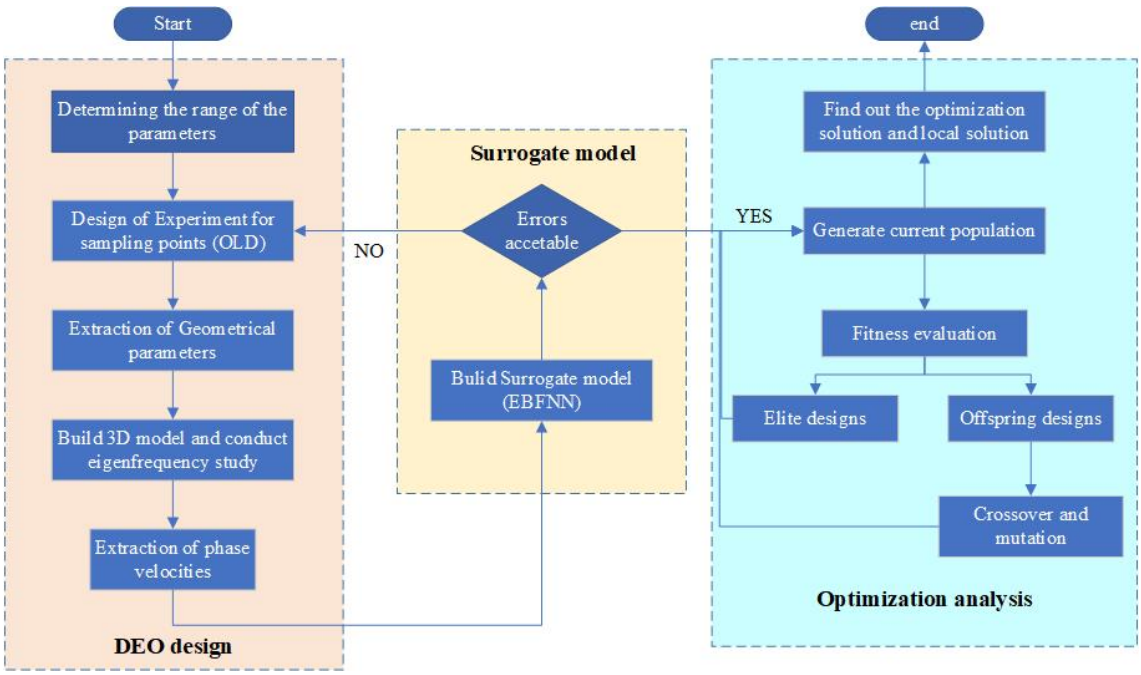

Figure 2: Detailed flowchart for optimization assisted by an elliptical basis function neural network and coupled with finite element simulations.

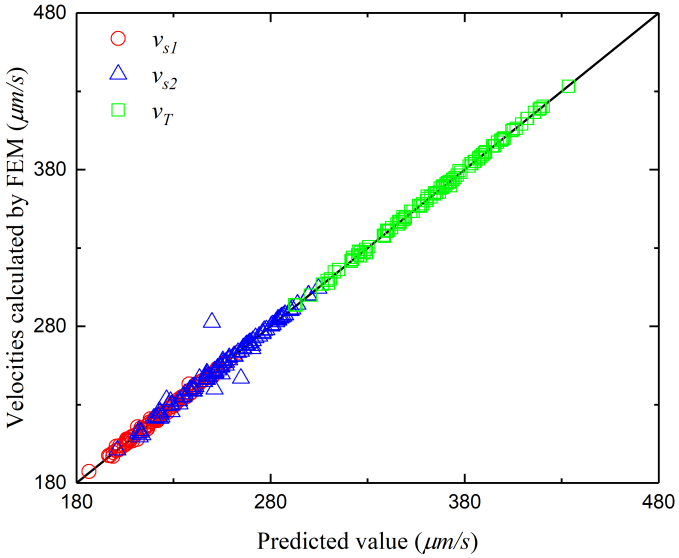

Figure 3: Comparison of velocities predicted by EBFNN with velocities obtained by FEM.

to be minimized are thus selected as

$$Iso(r_1, r_2, r_3, r_4) = |v_{S1} - v_{S2}|, \tag{16}$$

$$\upsilon(r_1, r_2, r_3, r_4) = \left| \frac{v_L^2 - v_{S1}^2 - v_{S2}^2}{2(v_L^2 - v_{S1}^2)} \right|. \tag{17}$$

Eigenfrequency study, performed by a commercial finite element software package (COMSOL Multiphysics), was adopted to calculate the required velocities. To ensure convergence of simulations, the truss lattice structures were modeled with several hundred of thousands of linear tetrahedral finite elements (type C3D10M). For the thinnest strut, there exist at least 10 elements around the circumferential direction. Bloch-periodic boundary conditions were imposed onto the representive unit cell shown in Fig.1. The constituent material chosen is assumed isotropic and linearly elastic with Young's modulus $E_0 = 2$ GPa, $\upsilon_0 = 0.4$, and mass density $\rho_0 = 1000\ \mathrm{kg \cdot m^{-3}}$.

The parameter space was sampled in order to reduce the computational burden during optimization. Toward this end, a surrogate model was created from a finite number of parameter space samples. One hundred sample points were first generated according to optimal Latin-hypercube design (OLD). This method was used to distribute sample points so that they are well spread over the design region without replicated coordinate values, often symmetric, and nearly optimal [49]. The generated sample points are listed in Table S1 of the Supplemental Material. A surrogate model was then generated and optimization was performed on the reduced parameter space, as described next.

Table 1: Accuracy measures of the EBFNN surrogate models.

Velocity	RMSE	R^2
v_{S1}	0.01546	0.99534
v_{S2}	0.0403	0.96955
v_L	0.00591	0.99934

3.2. Surrogate models

The elliptical basis function neural network (EBFNN) technique has proven effective in approximating a continuous function of n variables in very complex cases [50–52]. A detailed introduction to EBF is given in Ref. [53]. From the parameter space samples, a EBFNN was constructed to generate approximate surrogate models of the three velocities v_{S1}, v_{S2} and v_L.

The coefficient of determination (R^2) and the root mean square error (RMSE) are used to evaluate the reliability of the surrogate models. These estimators are defined as

$$R^2 = 1 - \frac{\sum_{i=1}^{n}(y_i - \hat{y}_i)^2}{\sum_{i=1}^{n}(y_i - \bar{y})^2}, \tag{18}$$

$$\mathrm{RMSE} = \sqrt{\frac{1}{n}\sum_{i=1}^{n}(y_i - \hat{y}_i)^2}. \tag{19}$$

In these expressions, n is the number of samples, y_i are the actual values of objective function at the sample points, $\hat{y}_i$ are the values predicted by the objective function, and $\bar{y}$ is the mean value of objective function over all sample points. All sample points defined by OLD are used for cross-validation error analysis. The closer R^2 is to 1 and RMSE is to 0, the more accurate the model. For all surrogate models, R^2 is larger than 0.969 and RMSE is smaller than 4%, as listed in Table 1. These values indicate that the surrogate models have high credibility. Fig. 3 compares

Table 2: Optimization results. Geometrical parameters, angular velocities in the [110) direction, and minimal and maximal values of Poisson's ratio υ for all compression directions are given for the initial and selected optimized designs.

structure	r_1 (μm)	r_2 (μm)	r_3 (μm)	r_4 (μm)	v_{s1} (μm/s)	v_{s2} (μm/s)	v_L (μm/s)	υ_{min}	υ_{max}
Initial	14.444	4.040	5.111	3.677	207.483	283.900	383.421	0.112	0.239
Optimum 1	15.000	4.500	5.100	2.400	218.590	219.256	323.220	0.076	0.077
Optimum 2	15.960	4.707	4.303	2.485	211.481	211.703	314.556	0.086	0.087
Optimum 3	15.535	4.121	4.909	2.222	198.819	201.040	293.675	0.067	0.073
Optimum 4	15.000	4.300	4.850	2.350	211.037	213.036	313.001	0.075	0.080

the velocities predicted by the surrogate models with the actual velocities, for all sample points. It can also be observed that the prediction error remains small in all cases. Of course, the usefulness of the surrogate models is to produce smooth estimates of the velocities for any continuous value of the quadruplet (r_1, r_2, r_3, r_4).

3.3. Optimization

Non-dominated sorting genetic algorithm (NSGA-II) [54] is used to find solutions to the optimization problem. Fig. 2 displays the optimization flowchart we follow. The current population of individuals contains two parts, the elite and the offspring points. In our case, its size is 12. As nondominated points, elites, that constitute not more than 50% of the population, are always inherited from the previous generation. In contrast, the offspring points are used for selection, crossover and mutation to generate the next generation. The probability of crossover and mutation are 0.9 and 0.1, respectively. Once the population is generated, a fitness evaluation is adopted to decide where design points go. Population update is continued until the maximum iteration number of 2000 is attained. To account for possible errors caused by the surrogate models, not only the optimum solution but also some local minima were extracted. By comparing simulations and optimization results, we picked up the four optimum designs listed in Table 2. Velocities and Poisson's ratios are estimated by conducting finite element simulations again after optimization.

Fig. 4 plots Poisson's ratio in spherical coordinates for both the initial and the optimum structure 1. The original structure proposed by Sigmund was indeed rather anisotropic, with the Poisson's ratio obtained by FEM varying between 0.112 and 0.239 depending on the direction. This may be attributed to the fact that the complex geometry of the nodes was not considered in the numerical algorithms used. In this case, actually, traditional truss or beam theories are not applicable. The mechanical properties ob-

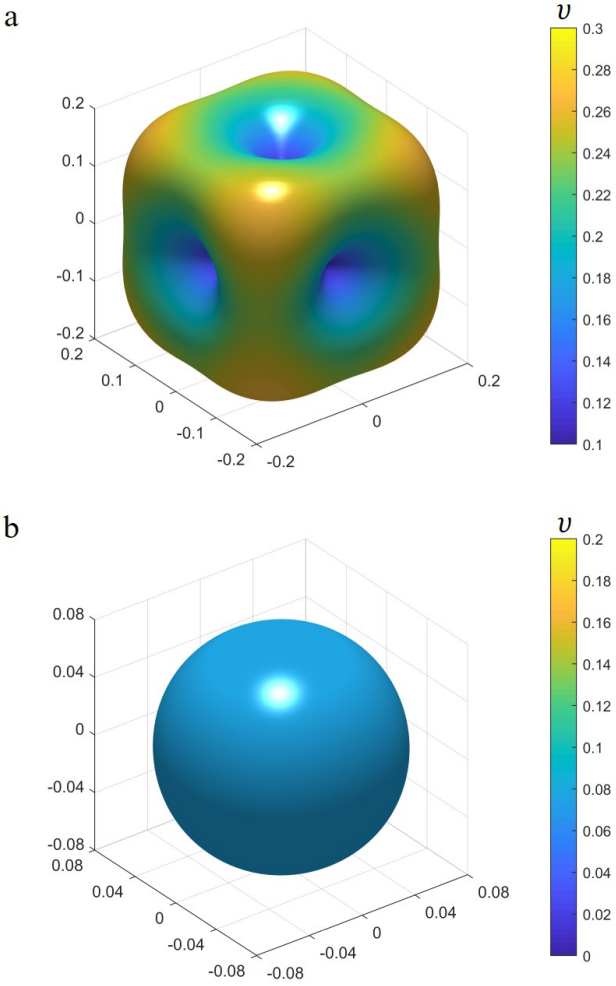

Figure 4: Three dimensional polar plot of the Poisson's ratio following by Eq. (9) for (a) the initial structure and (b) the optimal isotropic structure 1.

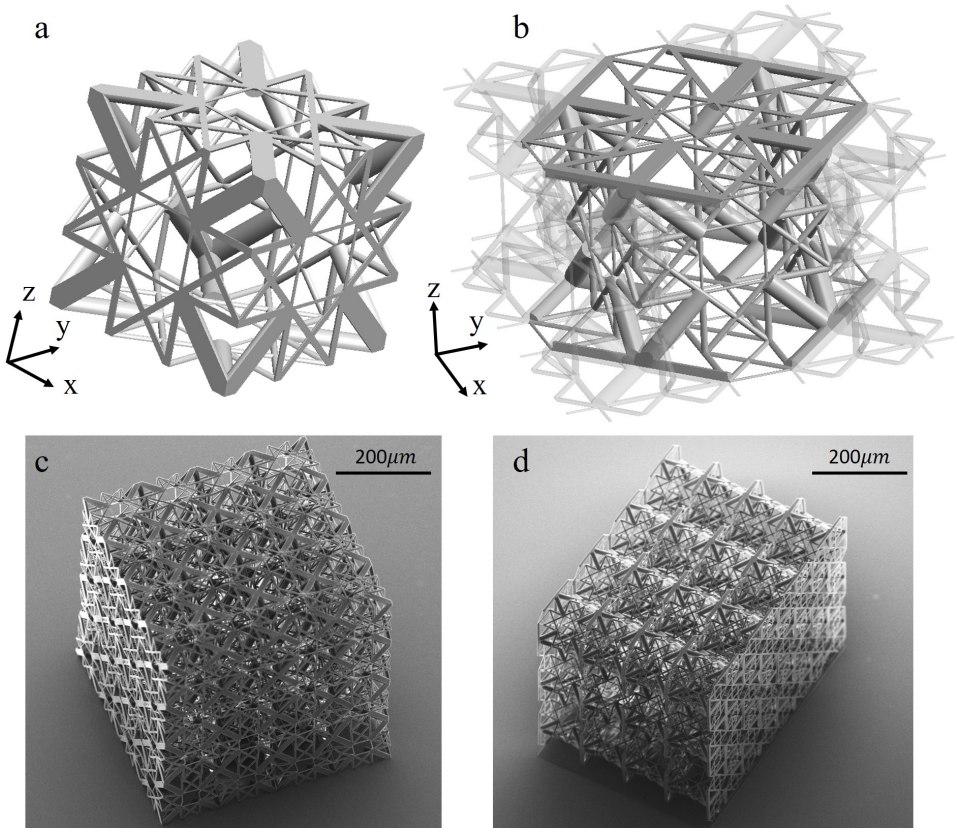

Figure 5: Unit cell models of the isotropic truss lattice material for (a) the [100] direction and (b) the [110] direction. Electron micrographs are shown for (c) the [100] fabricated sample with $4\times4\times4$ unit cells and (d) the [110] fabricated sample with $4\times4\times3$ unit cells.

tained by such methods differ significantly from the FEM result. Moreover, the minimum Poisson's ratio was larger than the upper bound for cork, 0.1. After optimization, an almost isotropic value $\upsilon \approx 0.08$ is obtained for the four selected designs. The response of the optimum structure is clearly much more isotropic than cork.

4. Experiment

All experimental samples are made from the 'IP-Dip' resin using the commercially available laser lithography system Photonic Professional GT (Nanoscribe GmbH, Germany). A drop of a negative-tone photoresist is placed on top of a fused silica substrate ($25 \times 25 \times 0.7$ mm^3) and polymerized using a femtosecond pulsed laser with vacuum wavelength λ = 780 nm. The laser beam is focused by using a dip-in ×63 objective lens with 1.4 numerical aperture. A Galvanometric scan speed of 10 m/s was used for the whole fabrication process. After polymerization is achieved, the sample is developed in PGMEA (1-methoxy-2-propanol actetate) for 20 minutes to remove the unexposed photoresist.

Two different crystallographic directions are considered, [100] and [110]. Fig. 5 shows the unit cell models and the corresponding additively manufactured samples. The [100] sample, which is composed of 4×4×4 unit cells, is constructed by stacking the corresponding unit cell in the three principal directions. Noting that the Poisson's ratio of lattice materials is mainly affected by the aspect ratio of micro-struts rather than by other geometrical parameters [8], we adopted the aspect ratios obtained from optimization and scaled the unit cell length proportionaly. The detailed geometrical parameters are: L = 125 μm, r_1 = 6.3 μm, r_2 = 1.9 μm, r_3 = 2.1 μm, and r_4 = 1 μm.

The [110] sample is generated by cutting out a [100] structure $2 \times 2 \times 1$ along the vertical direction. The horizontal basis vectors are then along directions

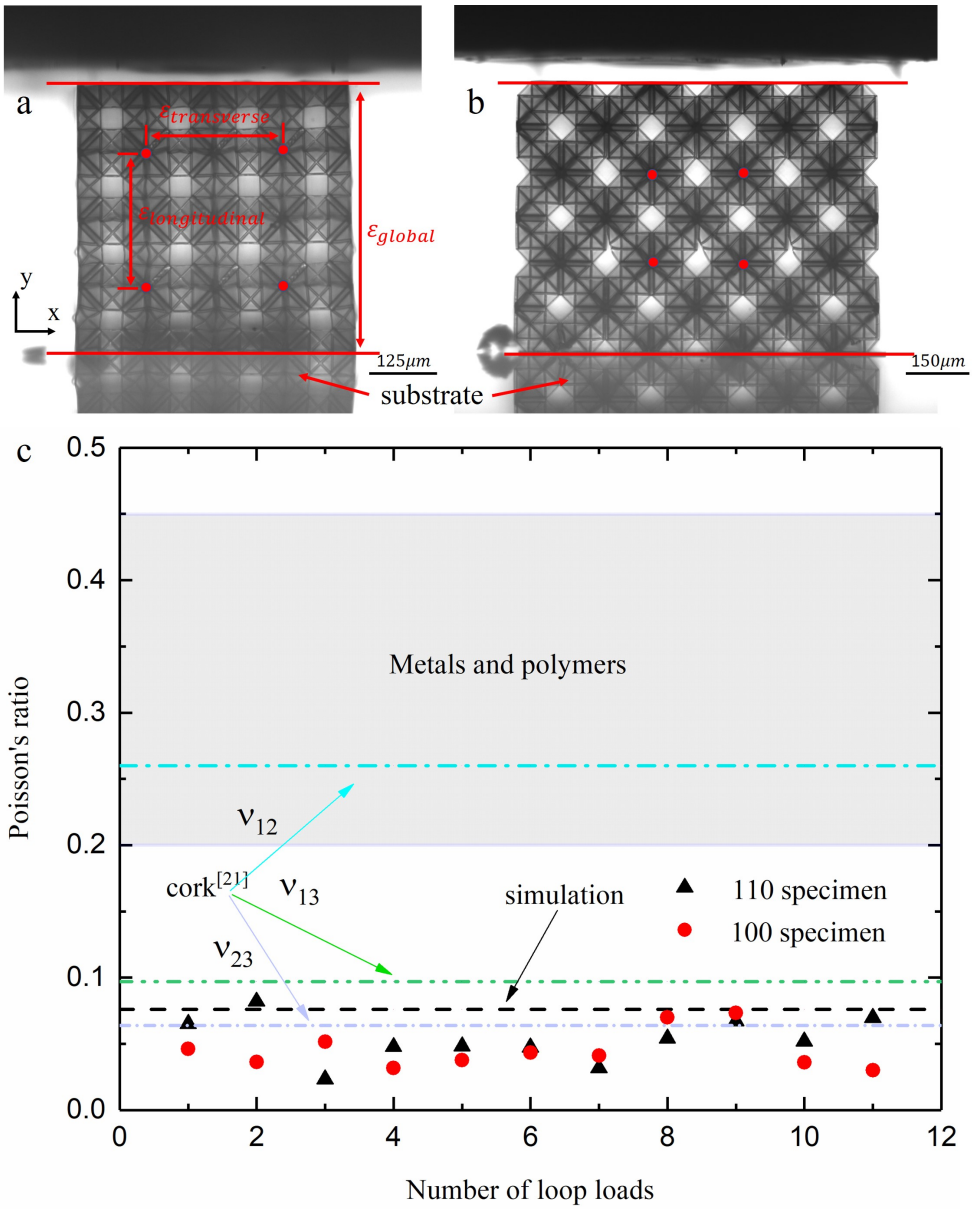

Figure 6: Definition of reference points and reference lines used to determine the transverse strain, the longitudinal strain and the global strain, for (a) the [100] sample and (b) the [110] sample. (c) Poisson's ratio of the samples is plotted as a function of the number of experimental loop loads. Values for the FEM simulation, cork, metals and polymers are shown for comparison.

[110] and [$\bar{1}$10]. It should be noted that the geometrical features of the [110] unit cell can be described by that of the corresponding [100] unit cell. Here, geometical parameters are L = 150 μm, r_1 = 7.6 μm, r_2 = 2.3 μm, r_3 = 2.5 μm, and r_4 = 1.2 μm. The [110] sample contains 4 × 3 × 4 unit cells. The external dimensions are 848.4 μm × 636.3 μm × 450 μm.

As shown in Fig. S1 of the supporting material, the samples are placed between a fixed glass substrate and a flat loading device. The loading device is driven by a stepping motor with an attached force sensor. Position is directly read from the linear stage. The position is only used to monitor the fatigue of the material. The true strain is obtained via image cross correlation. To test the recovery ability of the samples, repeated compressive experiments are carried out at a speed of 0.001 mm/s, during which the applied displacement increases with loop number. A digital camera equiped with a 20× objective lens facing the sample is used to monitor the deformation of the lateral faces and hence to measure Poisson's ra-

tio. Digital image correlation [55] is used to track and analyze the displacement with sub-pixel resolution. To reduce the influence of boundaries, Poisson's ratio is calculated from the average local strain and the average transverse strain measured from 4 reference circles at the central row of unit cells as depicted in Fig. 7. Fig. S2 details the measurement of coordinates. Green stars and red stars stand respectively for undeformed and deformation coordinates. At the initial position, green stars overlap with red stars. Table S2 lists representative data obtained from DIC for samples 100 and 110, where x and y stand for the original coordinates, and x' and y' are coordinates after deformation. The actual Poisson's ratio is calculated from the following expression,

$$\upsilon = -\frac{(x_2' - x_1' + x_4' - x_3') - (x_2 - x_1 + x_4 - x_3)}{(y_1 - y_3 + y_2 - y_4) - (y_1' - y_3' + y_2' - y_4')}. \tag{20}$$

Global strain is determined by measuring the distance between the reference lines.

Fig. 6(c) presents the measured Poisson's ratio of the [100] sample and the [110] sample. For both samples, experimental data are in fair agreement with simulation results of Table 2. The measurements are generally found to be smaller than the computed value. The contrast between samples shows that the proposed structure has a more isotropic response than cork and a much lower Poisson's ratio than other nature and man-made isotropic materials such as metals and Polymers. Moreover, the number of loop loading has a limited impact on the value of the Poisson's ratio. Even though some micro-struts break at large applied strain, the measured initial Poisson's ratio always fluctuates around the designed value of 0.076. For both configurations, the largest and the smallest Poisson's ratio measured in our cyclic experiments were about 0.08 and 0.025, respectively.

Fig. 7 summarizes the results of eleven cyclic compression experiments. A large vertical deformation together with a very small horizontal deformation are observed under compression, indicating that the structural materials have a nearly zero global Poisson's ratio. For both samples, the maximum applied strain increases almost linearly with the loop number. During the first and the last loop, the maximum strains of the [100] sample are 2% and 20%, respectively. As long as the applied strain remains smaller than 7%, the sample can recover completely after unloading (see Supporting movies 1 and 2). This property may be attributed to elastic buckling of the slender members in the micro-lattice. When the applied strain is increased above 7%, however, the recovery ability of sample weakens slightly. With a maximum applied strain of 20%, the sample can still recover almost 96.6% of its original height (see Supporting movie 4). In principle, the samples should possess even better recovery ability and should withstand larger strains. However, the slender micro-struts are very sensitive to flaws and imperfections. Hence the deformation of the sample may not be homogeneous and failure may start within any layer in the fashion of brittle break of the micro-struts (see Supporting movie 3). The compressive experiment validates our hypothesis. A similar trend regarding the recovery ability is found for the [110] sample (see Supporting movie 5). At large strain, brittle break of micro-struts is also the dominating failure mode of the tested sample (see Supporting movies 6 and 7). The only difference is that the recovery ability is further weakening. The [110] sample seems to be even more sensitive to flaws than the [100] sample. With a maximum applied strain of 16%, the [110] sample can almost recover 98.5% of its original height.

Compared with the original structure proposed by Sigmund, for which Poisson's ratio varies between 0.118 and 0.213, our structure is more isotropic. It would for instance make our structure more suitable as a bottle stopper. Moreover, our structure recovers 96.6% of its original shape after the 11th compressional test exceeding 20% strain. This mechanical behavior is attractive for product protection and goods packaging. When suffering from impact loading, limited stress can pass through the protection toward the product. The layer-by-layer buckling failure mode further enhances this protecting ability. Moreover, the recovery ability can save space for packaging which is important in aerospace applications. Compared with other traditional methods, our optimization method is simple and accurate. The optimization utilizing finite element simulation opens avenues for the design of 3D structures with

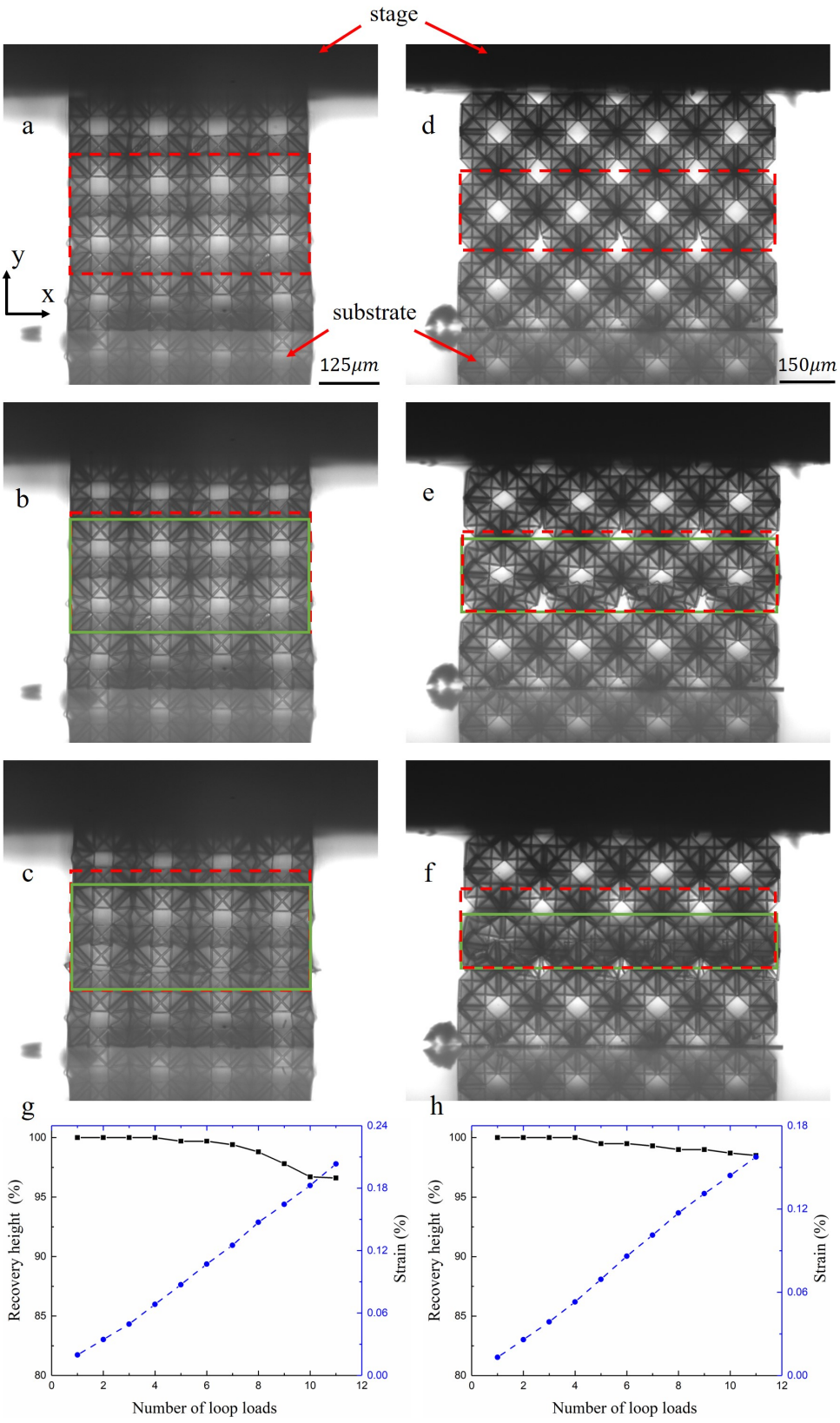

Figure 7: (a-c) Views of the deformed [100] sample at 0%, 5% and 10% strain. (d-f) Views of the deformed [110] sample at 0%, 5% and 10% strain. The red dashed square and the green solid square are the initial and the deformed shapes of samples, respectively. (g,h) Recovery ability of the [100] and the [110] samples and maximum applied strain as a function of the loop number.

very complex geometrical features, taking into account connected nodes, imperfections and so on.

5. Conclusion

A new class of isotropic reusable cork-like metamaterial with near-zero Poisson's ratio was designed using a multi-objective genetic algorithm assisted by an elliptical basis function neural network combined with finite element simulations. We derived an objective function for simultaneously imposing elastic isotropy and controlling the value of Poisson's ratio. The optimal structures were fabricated and tested under repeated compression experiments. Results show that the samples fabricated using two-photon lithography have an almost isotropic near-zero Poisson's ratio. Furthermore, they can almost recover 96.6% of their original shape after the eleventh compressional test exceeding 20% strain. The number of loop loadings has a limited impact on the value of Poisson's ratio. Even though some micro-struts break at large applied strain, the Poisson's ratio still fluctuates around the designed value.

Acknowledgments

This work was supported by Foreign Short-term Visiting Program for Doctoral Students at HIT. N.L., S.M., J.M., M.K. and V.L. acknowledge support by the EIPHI Graduate School (contract "ANR-17-EURE-0002") and the French Investissements d'Avenir program, project ISITE–BFC (contract ANR-15-IDEX-03). This work was partly supported by the french RENATECH network and its FEMTO-ST technological facility.

References

[1] S. Timoshenko, J. Goodier, Theory of elasticity (1970).

[2] G. W. Milton, A. V. Cherkaev, Which elasticity tensors are realizable?, Journal of engineering materials and technology 117 (4) (1995) 483–493.

[3] Y. Huang, X. Lu, G. Liang, Z. Xu, Pentamodal property and acoustic band gaps of pentamode metamaterials with different cross-section shapes, Physics Letters A 380 (13) (2016) 1334–1338.

[4] I. S. Sokolnikoff, R. D. Specht, et al., Mathematical theory of elasticity, Vol. 83, McGraw-Hill New York, 1956.

[5] H. Gercek, Poisson's ratio values for rocks, International Journal of Rock Mechanics and Mining Sciences 44 (1) (2007) 1–13.

[6] G. N. Greaves, A. Greer, R. S. Lakes, T. Rouxel, Poisson's ratio and modern materials, Nature materials 10 (11) (2011) 823.

[7] K. W. Wojciechowski, F. Scarpa, J. N. Grima, A. Alderson, Auxetics and other systems of "negative" characteristics, physica status solidi b 252 (7) (2015) 1421–1425.

[8] T. Bückmann, R. Schittny, M. Thiel, M. Kadic, G. W. Milton, M. Wegener, On three-dimensional dilational elastic metamaterials, New Journal of Physics 16 (3) (2014) 033032.

[9] G. Carta, M. Brun, A. Baldi, Design of a porous material with isotropic negative poisson's ratio, Mechanics of Materials 97 (2016) 67–75.

[10] X. Hou, H. Hu, V. Silberschmidt, A novel concept to develop composite structures with isotropic negative poisson's ratio: Effects of random inclusions, Composites science and technology 72 (15) (2012) 1848–1854.

[11] L. Cabras, M. Brun, A class of auxetic three-dimensional lattices, Journal of the Mechanics and Physics of Solids 91 (2016) 56–72.

[12] T. Frenzel, M. Kadic, M. Wegener, Three-dimensional mechanical metamaterials with a twist, Science 358 (6366) (2017) 1072–1074.

[13] T. Frenzel, J. Köpfler, E. Jung, M. Kadic, M. Wegener, Ultrasound experiments on acoustical activity in chiral mechanical metamaterials, Nature communications 10 (1) (2019) 1–6.

[14] M. C. Messner, Optimal lattice-structured materials, Journal of the Mechanics and Physics of Solids 96 (2016) 162–183.

[15] G. Gurtner, M. Durand, Stiffest elastic networks, Proceedings of the Royal Society A: Mathematical, Physical and Engineering Sciences 470 (2164) (2014) 20130611.

[16] J. Berger, H. Wadley, R. McMeeking, Mechanical metamaterials at the theoretical limit of isotropic elastic stiffness, Nature 543 (7646) (2017) 533.

[17] T. Tancogne-Dejean, M. Diamantopoulou, M. B. Gorji, C. Bonatti, D. Mohr, 3d plate-lattices: An emerging class of low-density metamaterial exhibiting optimal isotropic stiffness, Advanced Materials 30 (45) (2018) 1803334.

[18] C. Bonatti, D. Mohr, Mechanical performance of additively-manufactured anisotropic and isotropic smooth shell-lattice materials: Simulations & experiments, Journal of the Mechanics and Physics of Solids 122 (2019) 1–26.

[19] T. Tancogne-Dejean, D. Mohr, Elastically-isotropic truss lattice materials of reduced plastic anisotropy, International Journal of Solids and Structures 138 (2018) 24–39.

[20] T. Tancogne-Dejean, D. Mohr, Elastically-isotropic elementary cubic lattices composed of tailored hollow beams, Extreme Mechanics Letters 22 (2018) 13–18.

[21] S. Xu, J. Shen, S. Zhou, X. Huang, Y. M. Xie, Design of lattice structures with controlled anisotropy, Materials &

Design 93 (2016) 443–447.
[22] R. M. Latture, M. R. Begley, F. W. Zok, Design and mechanical properties of elastically isotropic trusses, Journal of Materials Research 33 (3) (2018) 249–263.
[23] L. Gibson, K. Easterling, M. F. Ashby, The structure and mechanics of cork, Proceedings of the Royal Society of London. A. Mathematical and Physical Sciences 377 (1769) (1981) 99–117.
[24] M. Fortes, M. T. Nogueira, The poison effect in cork, Materials Science and Engineering: A 122 (2) (1989) 227–232.
[25] G. Stavroulakis, Auxetic behaviour: appearance and engineering applications, physica status solidi (b) 242 (3) (2005) 710–720.
[26] J. N. Grima, R. Gatt, N. Ravirala, A. Alderson, K. E. Evans, Negative poisson's ratios in cellular foam materials, Materials Science and Engineering: A 423 (1-2) (2006) 214–218.
[27] X. Chen, Q. Ji, J. Wei, H. Tan, J. Yu, P. Zhang, V. Laude, M. Kadic, Light-weight shell-lattice metamaterials for mechanical shock absorption, International Journal of Mechanical Sciences 169 (2020) 105288.
[28] N. W. Bartlett, M. T. Tolley, J. T. Overvelde, J. C. Weaver, B. Mosadegh, K. Bertoldi, G. M. Whitesides, R. J. Wood, A 3d-printed, functionally graded soft robot powered by combustion, Science 349 (6244) (2015) 161–165.
[29] K. Bertoldi, P. M. Reis, S. Willshaw, T. Mullin, Negative poisson's ratio behavior induced by an elastic instability, Advanced materials 22 (3) (2010) 361–366.
[30] S. Babaee, J. Shim, J. C. Weaver, E. R. Chen, N. Patel, K. Bertoldi, 3d soft metamaterials with negative poisson's ratio, Advanced Materials 25 (36) (2013) 5044–5049.
[31] B. Florijn, C. Coulais, M. van Hecke, Programmable mechanical metamaterials, Physical review letters 113 (17) (2014) 175503.
[32] C. Coulais, E. Teomy, K. De Reus, Y. Shokef, M. Van Hecke, Combinatorial design of textured mechanical metamaterials, Nature 535 (7613) (2016) 529–532.
[33] N. Fang, D. Xi, J. Xu, M. Ambati, W. Srituravanich, C. Sun, X. Zhang, Ultrasonic metamaterials with negative modulus, Nature materials 5 (6) (2006) 452–456.
[34] X. Zheng, H. Lee, T. H. Weisgraber, M. Shusteff, J. DeOtte, E. B. Duoss, J. D. Kuntz, M. M. Biener, Q. Ge, J. A. Jackson, et al., Ultralight, ultrastiff mechanical metamaterials, Science 344 (6190) (2014) 1373–1377.
[35] T. A. Schaedler, A. J. Jacobsen, A. Torrents, A. E. Sorensen, J. Lian, J. R. Greer, L. Valdevit, W. B. Carter, Ultralight metallic microlattices, Science 334 (6058) (2011) 962–965.
[36] L. R. Meza, S. Das, J. R. Greer, Strong, lightweight, and recoverable three-dimensional ceramic nanolattices, Science 345 (6202) (2014) 1322–1326.
[37] O. Sigmund, Tailoring materials with prescribed elastic properties, Mechanics of Materials 20 (4) (1995) 351–368.
[38] D. Guth, M. Luersen, P. Muñoz-Rojas, Optimization of three-dimensional truss-like periodic materials considering isotropy constraints, Structural and Multidisciplinary Optimization 52 (5) (2015) 889–901.
[39] O. Rand, V. Rovenski, Analytical methods in anisotropic elasticity: with symbolic computational tools, Springer Science & Business Media, 2007.
[40] W. Voigt, Lehrbuch der kristallphysik: mit ausschlußd, Kristalloptik (Leipzig: BSB Teubner) (1910).
[41] V. Laude, Phononic Crystals: Artificial Crystals for Sonic, Acoustic, and Elastic Waves, De Gruyter, 2015.
[42] J. Christensen, M. Kadic, O. Kraft, M. Wegener, Vibrant times for mechanical metamaterials, MRS Communications 5 (3) (2015) 453–462. doi:10.1557/mrc.2015.51.
[43] L. J. Gibson, M. F. Ashby, Cellular solids: structure and properties, Cambridge university press, 1999.
[44] T. Tsang, H.-Y. Park, Sound velocity anisotropy in cubic crystals, Physics Letters A 99 (8) (1983) 377–380.
[45] R. Hill, The elastic behaviour of a crystalline aggregate, Proceedings of the Physical Society. Section A 65 (5) (1952) 349.
[46] A. Bower, Applied mechanics of solids (crc, boca raton, fl) (2009).
[47] K. W. Wojciechowski, Poisson's ratio of anisotropic systems, Computational methods in science and technology 11 (1) (2005) 73–79.
[48] T. Paszkiewicz, M. Pruchnik, P. Zieliński, Unified description of elastic and acoustic properties of cubic media: elastic instabilities, phase transitions and soft modes, The European Physical Journal B-Condensed Matter and Complex Systems 24 (3) (2001) 327–338.
[49] J.-S. Park, Optimal latin-hypercube designs for computer experiments, Journal of statistical planning and inference 39 (1) (1994) 95–111.
[50] C. Bishop, Improving the generalization properties of radial basis function neural networks, Neural computation 3 (4) (1991) 579–588.
[51] R. J. Schilling, J. J. Carroll, A. F. Al-Ajlouni, Approximation of nonlinear systems with radial basis function neural networks, IEEE Transactions on neural networks 12 (1) (2001) 1–15.
[52] M.-W. Mak, S.-Y. Kung, Estimation of elliptical basis function parameters by the em algorithm with application to speaker verification, IEEE Transactions on Neural Networks 11 (4) (2000) 961–969.
[53] L. Shi, B. Sun, Modeling and optimization of vibration response characteristics of the orbital sander based on surrogate model, Structural and Multidisciplinary Optimization 57 (6) (2018) 2259–2271.
[54] K. Deb, A. Pratap, S. Agarwal, T. Meyarivan, A fast and elitist multiobjective genetic algorithm: Nsga-ii, IEEE transactions on evolutionary computation 6 (2) (2002) 182–197.
[55] C. Eberl, R. Thompson, D. Gianola, S. Bundschuh, Digital image correlation and tracking with matlab, Matlab Central file exchange (2006).